WP15ER-PR(17) 18429

G Zvejnieks et al.

New intermediate asymptotic kinetics for a precipitate cluster growth in ODS steels: kinetic Monte Carlo studies

Preprint of Paper to be submitted for publication in
Acta Materialia

This work has been carried out within the framework of the EUROfusion Consortium and has received funding from the Euratom research and training programme 2014-2018 under grant agreement No 633053. The views and opinions expressed herein do not necessarily reflect those of the European Commission.

New intermediate asymptotic kinetics for a precipitate cluster growth in ODS steels: kinetic Monte Carlo studies

G. Zvejnieks*, A. Anspoks, E.A. Kotomin, V.N. Kuzovkov

Institute of Solid State Physics, University of Latvia, Kengaraga Str. 8, LV-1063 Riga, Latvia

Abstract

We have studied the cluster nucleation and growth kinetics in a simple oxide nano-sized aggregate formation model in oxide dispersion strengthened (ODS) steels using kinetic Monte Carlo (KMC) simulations. The KMC simulation results are extended to the experimentally relevant time range using autoregressive integrated moving average forecasting. We have simulated three prototypical (weak, medium and strong) interactions and defect concentration limits that are relevant for oxide nano-sized aggregate formation regimes and compared modeling with experimental results. In the long-time limit, we have observed the average defect cluster radius growth, $\overline{R} \sim t^{1/p}$ with $p = 3$, for a weak and (after a transition interval) for medium attractions predicted by the Lifshitz-Slyozov-Wagner (LSW) theory. However, the respective cluster growth rates in KMC simulations are overestimated as compared to the experimental rates. The best agreement with experiment is obtained for the strong interaction case, when nano-cluster growth occurs in a new *intermediate asymptotic* time scale regime without actually reaching the long-time limit predicted by the LSW theory. The strong interaction slows down the cluster growth rate, leading to a better agreement with experiment. Thus, our homogeneous nucleation model demonstrates that (i) the average interaction between defects in a real system is in between medium and strong interactions, and (ii) the oxide nano-clusters grow according to $\overline{R} \sim t^{1/p}$ in an intermediate asymptotic regime, during the typical experimental time scale, even up to several hundred of hours, with parameter p dependent on the average defect interaction and temperature.

Keywords: Oxide dispersion strengthened (ODS) steels, Nano-clusters, Coarsening, Ostwald ripening, kinetic Monte Carlo

1. Introduction

New alloy materials with improved radiation damage resistance at elevated temperatures are required for future fission and fusion reactors [1]. In particular, Fe-Cr based ferritic steels with ultra high concentration of Y-O (or Y-Ti-O) nano-clusters are promising candidates for such materials [2]. However, it is a technological challenge to produce an alloy with an uniform distribution of oxide nano-sized clusters. One of the possibilities is to perform the mechanical alloying (of steel and yttria) with the following thermo-mechanical treatment [3, 4]. There is a number of conditions in alloy processing that affect the final nano-cluster distribution, including: chemical composition of

*Corresponding author

Email address: guntars@latnet.lv (G. Zvejnieks)

the alloyed materials (in particular, the amount of Ti adatoms [5, 6]), temperature and duration of the annealing stage [7–12].

In recent years there was a growing interest to establish experimentally the oxide nano-cluster size kinetics. The time dependence of average cluster radius in the form, $\overline{R} \sim t^{1/p}$, with various power orders ($p = 3$ – LSW regime, 5 – pipe diffusion or ≈6) was proposed to interpret the experiments [7–12].

To understand the underlying processes, oxide nano-cluster formation and growth experimental studies where accompanied by extensive theoretical studies using *ab initio*, first principle KMC methods as well as thermodynamic approach, see e.g. [13–16]. KMC simulations were used to study Y_2O_3 precipitation kinetics in α-iron as well as the effect of supersaturation [13]. The effect of vacancies on mobility of Y, Zr, Ti atoms was also studied from first principles [14]. The dislocation pipe diffusion was proposed as a dominant mechanism in the semi-empirical thermodynamic and kinetic studies of oxide precipitation [15].

In this paper, using KMC simulations we study the precipitation process, starting from defect nano-cluster homogeneous nucleation till the cluster growth via Ostwald ripening mechanism, with a particular emphasis on the cluster growth kinetics. We use simplified Y_2O_3 formation model that allows us to make a direct quantitative comparison of an average cluster radii, cluster growth rate and cluster density with both available experimental data and other theoretical predictions. In the KMC simulations, we use *the standard model* and *the pair algorithm* approach [17] that was successfully applied earlier for studying complex kinetics both in 2D catalytic systems [18–20] and void self-organization in 3D [21]. In order to forecast aggregate growth kinetic results beyond the scope of KMC calculation limits, we complement the KMC simulations with the autoregressive integrated moving average (ARIMA) method [22].

2. Physical basis of the model

Let us summarize the experimental observations. The cluster structures arising in the ODS steels depend on the initial chemical composition of the material. On one hand, from the microscopic point of view the structures are determined by the defect types involved in the cluster formation and their interaction potentials. On the other hand, we are interested in the formation kinetics of non-equilibrium structures in a system of mobile and interacting defects. Formally, the kinetics of the microscopic model can be studied using KMC method. However, there are principal difficulties: The underlying physical process of defect aggregate formation is the Ostwald ripening. This phenomenon describes the time evolution of an inhomogeneous structure: small aggregates of defects dissolve and redeposit onto larger ones. The characterization of this process is of a particular interest in this study by approaching the long–time limit reflecting the fundamental laws of kinetics.

The studies of such asymptotics by KMC method is far from trivial. Ostwald ripening process is characterized by the time power law of $\overline{R} \sim t^{1/p}$ type, where $\overline{R}$ is the average aggregate radius, t - time and p - the power parameter. Therefore, to obtain the non-redundant information, the time interval of data sampling should increase exponentially and simulation time should cover several orders of magnitude. With such a sampling, the number of large aggregates, that are the primary objects of interest, is decreasing approximately exponentially in the systems with Ostwald ripening in the long–time limit, the statistics is respectively worsening. For example, in order to extend

the simulations with a few large clusters left for approximately three (exponential) steps, one needs to increase twice the lattice size. As the result, the computer time required for simulations increases 2^3 times. One can propose naively to extrapolate to the long–time limit of KMC simulations using LSW theory [23, 24]. This approach, however, has some shortcomings. On one hand, the LSW theory operates with two competitive concepts of diffusion and reaction. Defect interactions are incorporated in the theory indirectly by using macroscopic surface tension and reaction rate. (In general a surface tension might depend on the size of the clusters and position of parameters in the phase diagram [25]). Then, the theory predicts different Ostwald ripening behavior in the long–time limit for either diffusion, $\overline{R} \sim t^{1/3}$, or reaction limited, $\overline{R} \sim t^{1/2}$, cases, respectively. It is predicted that the proportionality coefficients depend on solubility concentration and thus the rates are independent of total defect concentration in the system.

On the other hand, the KMC simulations are based on the microscopic model with a given defect interaction, concentration and temperature. The surface tension originates from attractive defect interactions that lead to formation of clusters and is not introduced directly in the model. Moreover, no assumption is made regarding the slowest process and the KMC simulations allow to study the defect concentration effects. The topmost advantage is that KMC allows us to explore the whole process of defect aggregate formation, starting from nucleation till Ostwald ripening regime, and determine the intermediate asymptotic kinetics that might arise before reaching the LSW long–time limit. In such the case, the asymptotics corresponds to the auto-model solution between two limiting parameter values (for certainty – two times t_{min} and t_{max}). In other words, when observation time, t, is larger than t_{min} but shorter than t_{max}, the characteristic distributions are obtained using similarity transform. Correspondingly, the kinetics of the process is characterized by fundamental time power laws [26, 27].

Importance of the intermediate asymptotic is due to the following specific features of the ODS steel experiments: a few nanometer large aggregates typically grow during a few hours (or a few hundred of hours in dedicated kinetics studies) and at the same time, the aggregates grow with time follows a power order, $t^{1/5}$ or $t^{1/6.28}$ [11] that was interpreted as the result of pipe diffusion. However, as shown in this paper, similar power orders could arise also as an intermediate asymptotic before reaching the LSW regime. These results hold for a simple 3D model with defect diffusion and interaction, without any other (e.g., pipe) diffusion mechanism.

In the KMC simulations of intermediate asymptotics, developement of the detailed microscopic model could cause substantial difficulties. Such a model requires knowledge of all the elementary microscopic processes including all types of relevant defects, their interactions and mobility parameters and is actively developed during last years, see [13–16].

On the one hand, such an approach with interactions estimated from the first-principle calculations [28, 29] when used in KMC simulations [20] might lead within the uncertainty of parameters to a wide variety of system behaviors. On the other, precise interaction energies between defects determine mainly the short-range order or defects within the aggregates rather than the asymptotic time dependence of average aggregate radius. Therefore, in this paper, we simplify the process of detailed Y_2O_3 aggregate formation in ODS steels and study the fundamental aggregate growth laws, depending on defect interaction, temperature and concentration. Our model is complementary to traditional studies of detailed microscopical treatments but is focused on the cluster formation kinetics.

3. Model

The detailed models that take into account different types of defects (Y, Ti, O and Fe vacancies), their microscopic interactions and diffusion where used in previous KMC simulations [13, 30–32]. In this paper we focus on the intermediate– and long–time kinetics of the aggregate growth.

Our simplified model is based on the following assumptions. (i) Inter-defects interaction energies affect mainly the short-range order in clusters. However, we are interested in the kinetics of aggregate growth that is governed by the defect transport. Therefore, in the present study we consider the yttria nano-clusters as an object without the inner structure, that is formed by the effective defects which are indistinguishable and can be characterized by an effective interaction. Formally, we treat Y, O atoms and Fe vacancy each as a single defect A with all interactions reduced to the average NN interactions with energy ε.

Let us estimate the concentration of effective defects A that are required to create an Y_2O_3 bixbyite structure (lattice constant 1.06 nm [33] and atomic weight $A_{Y_2O_3} = 226$ u) within the α-iron lattice (lattice constant a_0=0.286 nm [34] and $A_{Fe} = 56$ u). Formally, this step requires additional Fe vacancies [35], to be built-in nano-cluster, that finally leads to $Y_2O_3\mathrm{Vac}_3^{Fe}$ complex (unit) that occupies 8 Fe body-centered cubic (bcc) lattice sites in α-iron.

A typical Y_2O_3 concentration in ODS steels is 0.3 wt % that could be transformed to Y_2O_3 unit concentration per site (occupancy) according to

$$c_{Y_2O_3} = \frac{0.3wt\%/A_{Y_2O_3}}{0.3wt\%/A_{Y_2O_3} + 99.7wt\%/A_{Fe}}\,. \tag{1}$$

In our KMC we assume that A defect concentration $c_A = 8\,c_{Y_2O_3}$ since Y_2O_3 occupies 8 sites in the bcc lattice. For a typical experimental Y_2O_3 concentrations of 0.3 wt % mentioned above this corresponds to occupied site concentration $c_A = 0.006$. Additional impurity atoms have negligible effect on site concentration. (For example, when 0.1Ti is added to the system, the concentration per site might increase till $c_A \sim 0.007$ if Ti doesn't build into Y_2O_3 structure and each Ti atom requires additional bcc Fe site. Contrary, if Ti builds into the Y_2O_3 structure, the concentration per site remains unchanged.) For a completeness of definition, let us introduce also a monomer concentration, c_0', by excluding the volume of all clusters (where number of defects ≥ 2).

(ii) The model is complemented by the kinetic part. The aggregation kinetics is governed by both – defect interactions and the transport of defects to and from the aggregates. Various defects have distinct mobilities and they affect aggregation kinetics in different ways. For example, it is known that Y defect diffusion is the slowest while mobilities of Fe vacancies, Ti and O are much faster. Thus Y defect transport and two Y defect en-counting is a limiting step for Y_2O_3 cluster nucleation and growth in the α-iron matrix. Contrary, Fe vacancies, Ti or O defects are incorporated into nano-clusters much faster due to their higher mobility, that in turn has no effect on nano-cluster growth kinetics. Therefore, we set the effective defect A diffusion equal to that of Y atoms.

Defect A jumps to the NN empty lattice site are characterized by the diffusion coefficient

$$D = D_0 \exp[-E_{act}/(k_BT)] = l^2\nu/z = l^2\nu_0/z \exp[-E_{act}/(k_BT)]\,, \tag{2}$$

where l is jump length, z number of NN and ν_0 attempt frequency. In the bcc lattice with eight nearest neighboring sites ($z = 8$) the jump length is $l = \sqrt{3}a_0/2$, where a_0 is the α-iron lattice constant.

D_0 [m^2/s]	E_{act} [eV]	ν_0 [s^{-1}][c]	$\nu(1100°C)$ [s^{-1}]
10^{-5}	3.10[a]	10^{15}	4×10^3
8.0×10^{-7}	2.26[b]	10^{14}	5×10^5

Table 1: Experimental[a] [13, 36] and calculated[b] [14] mobility parameters for Y defects in α-iron. [c]Estimates of attempt frequencies are obtained from Eq. (2) using D_0 and E_{act}.

Experimental and theoretical Y defect diffusion coefficient estimates (and the hopping rate) in α-iron matrix, Table 1, differ by two orders of magnitude at the experimentally relevant temperature 1100 °C of oxide nano-cluster formation regime. In KMC simulations the hopping rate only rescales time, see the simulation algorithm below, thus in this paper for certainty we use the hopping rate estimate by Alinger and Hin [13, 36].

In computer simulations, we consider bcc lattice of size $L\times L\times L = V$ (where L is lattice side length which varies from $L = 80$ till $240a_0$) with $N = 2V/a_0^3$ sites and periodic boundary conditions. Defects A are distributed randomly within the lattice at the beginning of simulations. Defects are mobile and can hop to the nearest free site. This step is implemented in KMC simulations using *the pair algorithm* and *the standard model dynamics* [17]. The pair algorithm contains the following steps:

- A NN pair is randomly selected from all possible pairs in the bcc lattice.
- If the pair contains a single vacancy and A defect (OA or AO), the hoping step (exchange of positions AO or OA, respectively) is performed, if a random number (RN) normalized to unity is less that step rate, $\nu_{\alpha\beta}$,

$$\nu_{\alpha\beta} = \frac{2\nu}{1+\exp\left(-(n_\alpha - n_\beta)\varepsilon/(k_BT)\right)}, \tag{3}$$

  where α and β are the first and second site of the pair. The jump rate of a single free defect, ν, from Eq. (2) is modified in Eq. (3) to take into account the interaction between defects. The standard model dynamics [17] allows us to introduce the step rate symmetrically (irrespective of the direction of the jump, e.g, $OA\rightleftharpoons AO$) unlike to, e.g., the Metropolis dynamics [37]. The negative interaction energy used for a pair of defects in NN positions, ε, corresponds to their mutual attraction; n_α and n_β are the numbers of occupied NN positions in the initial and final configurations, respectively. Here it is convinient to introduce a dimensionless interaction energy $\epsilon = \varepsilon/(k_BT)$.
- Time is updated by a fixed increment

$$\Delta t = \frac{1}{N\nu} \tag{4}$$

  and the algorithm returns to the first step, until the final simulation time is reached. In the KMC simulations, we use dimensionless time $\tau = t\nu$ and return to dimensional time, t, only when we make a comparison with experimental results.

The long-time behavior (LSW-type power laws) are examined in KMC at the temperature 1100 °C for three particle concentrations, c_A (0.2, 0.1, and 0.005), and three interaction energies, ε: weak (-0.1), medium (-0.3), and strong (-0.5 eV) that correspond to the dimensionless interactions $\epsilon = -0.85$, -2.54, and -4.23, respectively. In order to increase the accuracy of KMC simulations, we repeat and average results of 10 calculations, unless specified otherwise.

4. KMC simulation analysis

4.1. Phase diagram

In order to analyze the spatial defect structures, we define a defect cluster as a connected (in nearest neighbor (NN) sense) group of A defects in the bcc lattice. Cluster formation strongly depends on both, A defect concentration, c_A, and dimensionless interaction energy, ϵ, as shown in the solubility-supersolubility diagram, Fig. 1. Similarly to Ref. [38], we find here three zones: (i) the stable (unsaturated) zone where spontaneous nucleation and cluster growth is impossible; (ii) The metastable (supersaturated) zone, where spontaneous nucleation is improbable, but a cluster seed placed in the metastable zone would experience growth; (iii) The unstable (supersaturated) zone, where spontaneous nucleation is probable, but not inevitable.

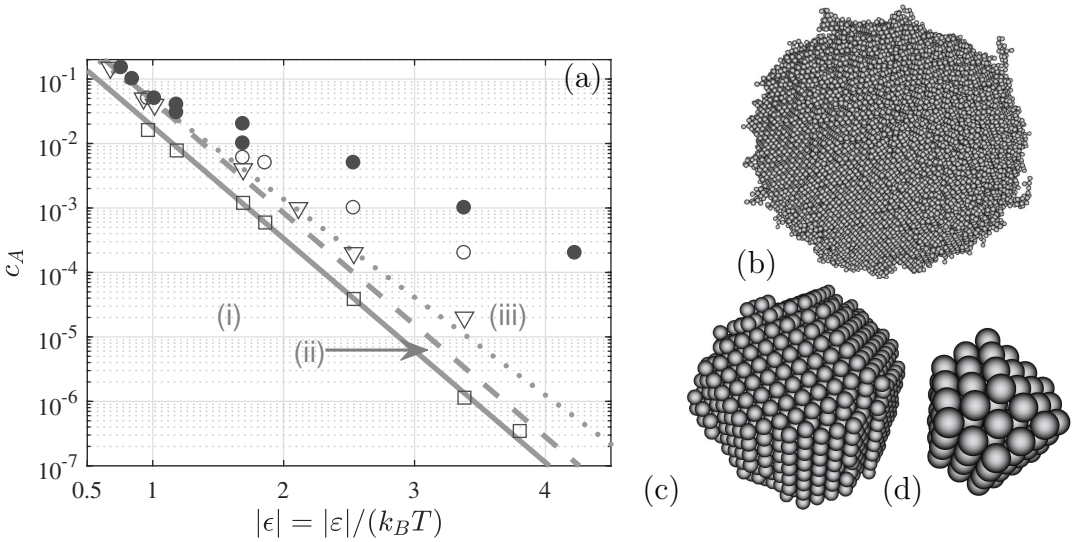

Figure 1: Solubility–supersolubility phase diagram (a). Three zones could be distinguished: (i) the stable, (ii) the metastable and (iii) the unstable. KMC simulations demonstrate defect aggregation (full circles), single large cluster growth (open circles), and no cluster growth regimes (down triangles), respectively. Solubility estimates from KMC, c_∞^{GT}, are given by squares. A solubility, $c_\infty^A(\epsilon)$, and two supersolubility, $c_{nuc}(\epsilon)$, fit to the Arrhenius equations are shown by solid and dashed/dotted lines, respectively. Snapshots of average cluster size, r_n, Eq. (7), for (b) weak ($\epsilon = -0.85$) $r_{105866} = 6.7$ nm, (c) medium ($\epsilon = -2.54$) $r_{1801} = 1.7$ nm and (d) strong ($\epsilon = -4.23$) $r_{123} = 0.7$ nm interactions at time $\tau = 3.3{\times}10^6$ and defect concentration c_A=0.1. Each data point is obtained from a single KMC calculation.

The solubility concentration, $c_\infty(\epsilon)$, that separate the stable-(i) and the metastable-(ii) zone can be found from KMC simulations that lead to an equilibrium configuration with a single spherical cluster with a radius, r, surrounded by single defects (flow of defects to and from the cluster are equal). KMC simulations that give such a configuration, might bypass the Ostwald ripening stage when just a single nucleus (and thus a single cluster) is created in the lattice often after a prolonged incubation period, see empty circles in Fig. 1. The solubility concentration, $c_\infty^{GT}(\epsilon)$, can be estimated using the equilibrium monomer concentration, $c_0'(\tau \to \infty)$, at a single spherical cluster by excluding the volume of the

cluster and the well-known Gibbs–Thomson relation [39]

$$c_0'(\tau \to \infty) = c_\infty^{GT}(\epsilon) \exp\left(\frac{l_c}{r}\right), \text{ where} \tag{5a}$$

$$l_c = \frac{2\gamma v_1}{k_B T}, \tag{5b}$$

$$\gamma = \frac{(z_s - z_b)\varepsilon}{2s_1}, \tag{5c}$$

$$c_\infty^A(\epsilon) = c_\infty^0 \exp(-k_\infty|\epsilon|), \tag{5d}$$

where l_c is the capillarity length and v_1 volume of a single defect. The specific interfacial energy, γ, using a simplified bond-counting model could be estimated from Eq. (5c), where s_1 is a single-defect exposed surface area, z_s and z_b are numbers of occupied bonds for a defect at the surface and in the bulk of the cluster, respectively. For compact clusters formed by {110}–facets (Fig. 1c,d) the number of bonds can be estimated as $z_s = 6$ and $z_b = 8$, respectively, that, in turn, leads to a surface area, $s_1 = \pi r_1^2$. The solubility $c_\infty^{GT}(\epsilon)$ estimates obtained using Eqs. (5a–5c) are shown by square symbols in Fig. 1. On the other hand, the solubility concentration, $c_\infty(\epsilon)$, can be estimated in the Arrhenius form Eq. (5d) [40], where $c_\infty^0 = 1.0$ and $k_\infty = 4.0$, see solid line in Fig. 1. (The c_∞^0 coincides with the bulk concentration in the $T \to \infty$ limit, while $k_\infty = 4.0$ corresponds to half of the bcc lattice coordination number [40].) Both estimates agrees well, $c_\infty(\epsilon) \equiv c_\infty^{GT}(\epsilon) = c_\infty^A(\epsilon)$, indicating that Eqs. (5) are self-consistent, except for weak interactions, $|\epsilon| < 1$. In the latter case the defect cluster is loose, see Fig. 1b, and the simple interfacial energy estimates Eq. (5c) are no longer applicable, since for diffuse clusters there exist no simple estimate of the occupied surface bound number, z_s, and exposed defect surface, s_1.

Determination of metastable-(ii) and the unstable-(iii) zone separation (the supersolubility curve) is more challenging, since its position, among other things, is affected by the history of the sample [38]. In KMC simulations we find that weak attraction and small concentration strongly suppress cluster nucleation and thus hinder the reaching of the critical cluster size, see down-triangles in Fig. 1. Moreover, there is a region in the unstable zone where just a single defect cluster is formed in the lattice after a certain incubation time, see open circles in Fig. 1. The incubation time increases either by approaching the supersolubility curve in the phase diagram and/or by decreasing the lattice size. The supersolubility curve, $c_{nuc}(\epsilon)$, can be estimated in the Arrhenius form

$$c_{nuc}(\epsilon) = c_{nuc}^0 \exp(-k_{nuc}|\epsilon|), \tag{6}$$

however, with some uncertainty. Here we define that there is no spontaneous nucleation in a KMC simulation run, when for a 3D lattice of size, $L = 120a_0$, nothing happens during $\tau = 4{\times}10^6$ (16 min at 1100 °C). It should be noted, that larger lattice sizes or longer waiting times can still initiate nucleation. Then for the supersolubility approximation Eq. (6) there are two extremes: (i) a more conservative approach – when $c_{nuc}(\epsilon)$ is proportional to $c_\infty(\epsilon)$ with $c_{nuc}^0 = 2.5$ and $k_{nuc} = 4.0$ (dashed line in Fig. 1), (ii) less conservative approach, that is based on our definition of absent-nucleation in KMC simulations, then leads to the parameters $c_{nuc}^0 = 1.5$ and $k_{nuc} = 3.5$ (dotted line in Fig. 1).

Defect nucleation and growth takes place in the KMC simulations when the starting random distribution of A defects exceeds the supersolubility curve, $c_A \approx c_0'(\tau = 0) > c_{nuc}(\epsilon)$, for a given interaction energy, ε, and temperature, T, see phase diagram (full

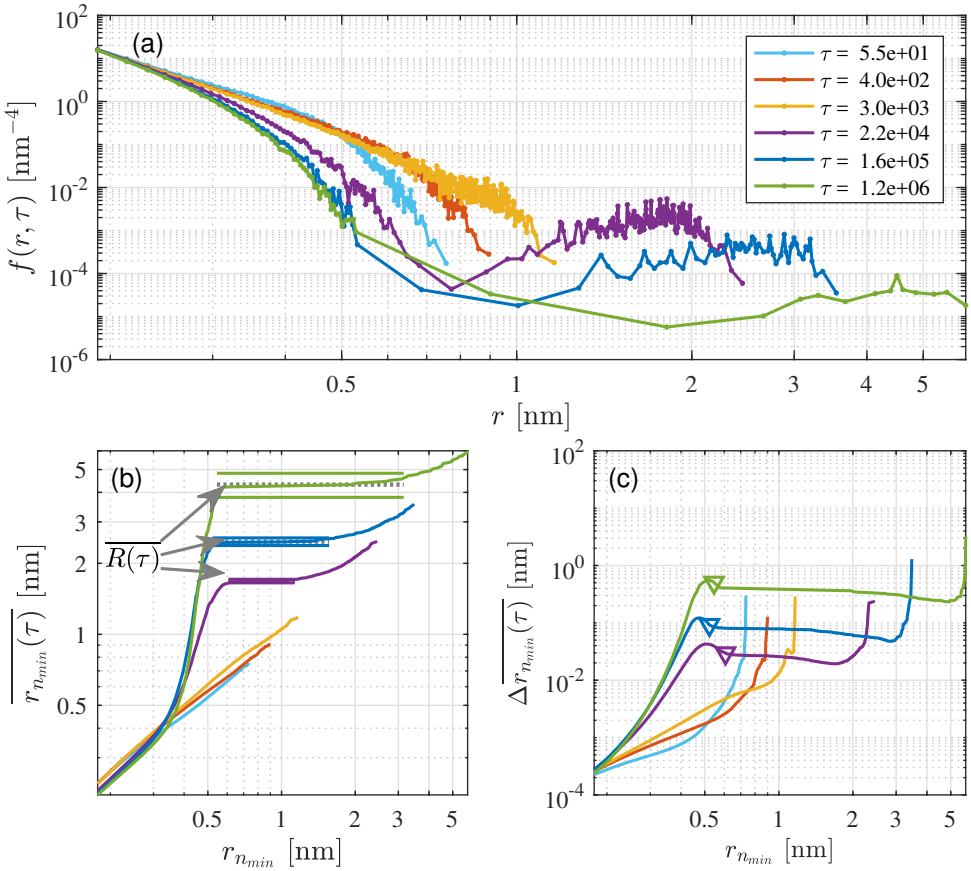

Figure 2: Cluster density analysis in the limit of weak attraction, $\epsilon = -0.85$: (a) PDF, (b) average cluster radius dependence on n_{min} (n_{min} independent average cluster radius, $\overline{R(\tau)}$, marked as dotted gray lines), and (c) accuracy of average cluster radius estimates. $\overline{R(\tau)}$ accuracy estimate marked by down triangles in (c) and plotted as a horyzontal lines in (b). Data are obtained from a single KMC simulation with parameters: $L = 240a_0$, $c_A = 0.1$, $\varepsilon = -0.1$ eV, $T = 1100$ °C.

circles) in Fig. 1. It should be noted that the largest concentration that could be randomly distributed in the bcc lattice without formation of percolating cluster, $c_A \lesssim 0.18$ (the bond percolation threshold [41]). For subpercolation concentrations two scenarios are possible with the advance of time – nucleation still continues if the remaining monomer concentration (taking into account the cluster excluded volume) is sufficient, $c_0'(\tau) > c_{nuc}(\epsilon)$. However, if the monomer concentration decreases below the supersolubility limit, $c_0'(\tau) < c_{nuc}(\epsilon)$, the nucleation is suppressed. In the latter regime, the existing clusters could grow on the expense of either other clusters (Ostwald ripening) or, in a case of a single cluster, on other monomers if $c_0'(\tau) > c_0'(\tau \to \infty)$.

4.2. Defect distribution function

Let us now quantitatively analyze the cluster growth in the unstable-(iii) zone. By performing the cluster analysis we find sizes, n, of each cluster in the lattice at time, τ. Due to two atoms in the bcc unit cell, we can estimate the cluster volume as $v_n = n\,a_0^3/2$. Then assuming that a cluster of n defects has a spherical shape, the corresponding cluster radius could be found as

$$r_n = \left(\frac{3n}{8\pi}\right)^{1/3} a_0\,. \tag{7}$$

The number of clusters is examined using the defect distribution function, $f(r,\tau)$,

(PDF) [24]. The PDF is a discrete function due to an integer number of defects in a cluster, n, see Eq. (7):

$$f(r,\tau) = \{f(r_1,\tau), f(r_2,\tau), \ldots, f(r_{n_{max}},\tau)\}\,, \text{ where} \tag{8a}$$

$$f(r_n,\tau) = \frac{1}{V}\lim_{\Delta r_n \to 0} \frac{M\left(r_n, r_n+\Delta r_n, \tau\right)}{\Delta r_n}\,, \tag{8b}$$

and $M\left(r_n, r_n+\Delta r_n, \tau\right)$ is the number of clusters in volume, V, having radii, r, between r_n and $r_n+\Delta r_n$ at time τ. For the PDF calculation the bin sizes Δr_n in Eq. (8b) on the one hand should be as small as possible, while on the other hand they should contain a sufficiently large number of clusters, to reduce the statistical error. In our PDF estimate, each individual bin size is increased adaptively, till it contains at least two clusters, $M \geq 2$, that ensures the PDF continuity and smoothness, Fig. 2a, especially for large radius values.

The average cluster size can be defined as the first momentum, using Eqs. (7,8b)

$$\overline{r_{n_{min}}(\tau)} = \frac{\int r f(r,\tau) dr}{\int f(r,\tau) dr} = \left(\frac{3}{8\pi}\right)^{1/3} a_0 \frac{\sum\limits_{n=n_{min}}^{n_{max}} n^{1/3} M\left(r_n,\tau\right)}{\sum\limits_{n=n_{min}}^{n_{max}} M\left(r_n,\tau\right)}\,, \tag{9}$$

where the last term here is independent on the bin size Δr. Radius at n_{max} should account for the largest cluster in the lattice, but selection of n_{min} is a non-trivial task [25] and will be discussed below. The classical rate theories that estimate time dependence of average cluster radius neglect the cluster nucleation and coalescence [42]. However, nucleation is intrinsic process in KMC simulations that is observed in PDF as a number of small-radii clusters, see, Fig. 2a, when scaled monomer concentration, c_0', exceeds the supersolubility concentration, $c_{nuc}(\epsilon)$, in Fig. 1. The shape of PDF remains qualitatively the same, untill $\tau = 3{\times}10^3$, when only PDF width increases with time, indicating that the average cluster radius increases. However, after this incubation time, the shape of PDF qualitatively changes, from $\tau = 2.2{\times}10^4$ in Fig. 2a, when the group of large clusters emerges and is observed as a second maximum in the PDF. These clusters grow further according to the Ostwald ripening rules and will be in the focus of our further analysis. The contribution of small clusters in the PDF thus should be ignored. We achieve this goal by neglecting the cluster sizes smaller that n_{min}.

In order to set the n_{min}, let us first determine the $\overline{r_{n_{min}}(\tau)}$ dependence on $r_{n_{min}}$. The average cluster radius increases as clusters with sizes smaller than n_{min} are excluded from averaging in Eq. (9), Fig. 2b. Finally, the plateau regions (if present) in $\overline{r_{n_{min}}(\tau)}$ figure correlate with the minima of PDF function, Fig. 2a, and can be used as the n_{min} independent average cluster radius estimates by excluding the nucleation contribution

$$\overline{R(\tau)} = \lim_{n_{min}} \overline{r_{n_{min}}(\tau)} \approx const\,. \tag{10}$$

When no such plateau region exists, e.g., during the incubation time, we assume that no characteristic cluster size exists in the system. The accuracy of the average cluster radius for each $r_{n_{min}}$ can be estimated using the standard deviation, S, and Student's two–sided

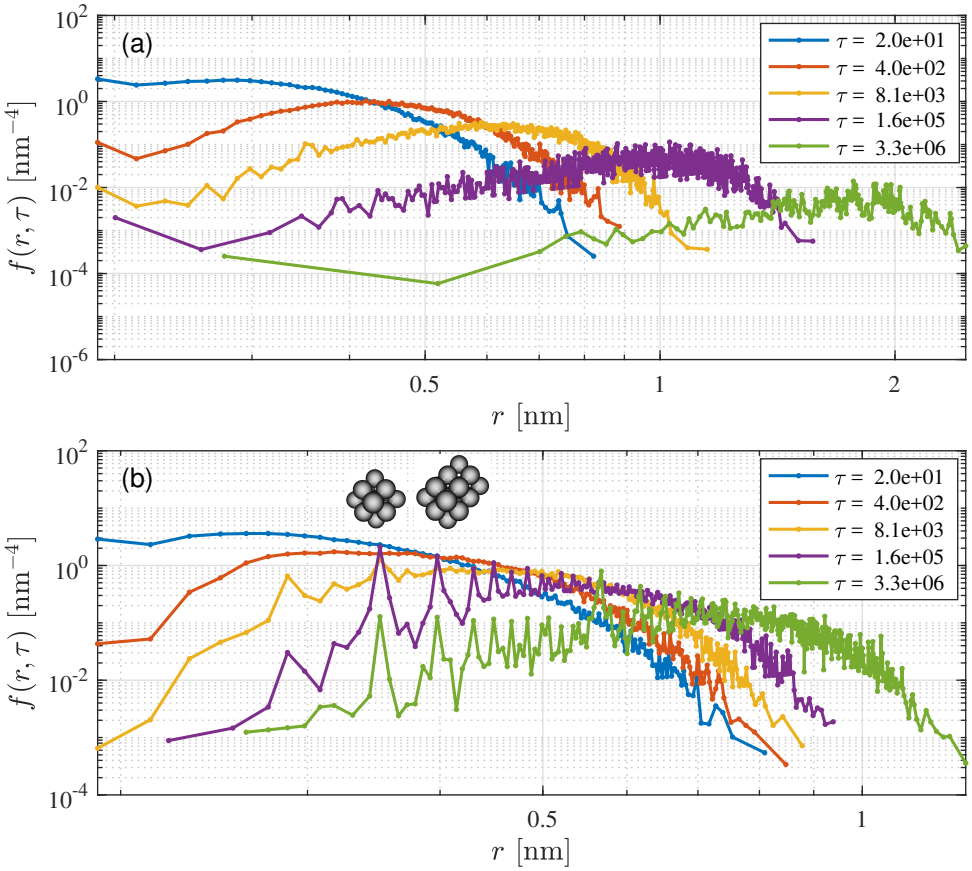

Figure 3: PDF for attractive: (a) medium, $\epsilon = -2.54$, and (b) strong, $\epsilon = -4.23$, interactions. Long living stable clusters of magic numbers $n = 15$ and 22 corresponding to the maxima of PSD functions at $r_{15} = 0.35$ and $r_{22} = 0.39$ nm at $\tau = 1.6{\times}10^5$ and $3.3{\times}10^6$, respectively are shown in insets of (b). Data are obtained as average over 10 independent KMC simulation with parameters: $L = 80a_0$, $c_A = 0.1$, $\varepsilon = -0.3$ (a) and -0.5 eV (b), $T = 1100$ °C.

t-distribution [43],

$$S = \sqrt{\frac{1}{n_{max} - n_{min}} \sum_{n=n_{min}}^{n_{max}} (r_n(\tau) - \overline{r_{n_{min}}(\tau)})^2}\,, \tag{11a}$$

$$\Delta\overline{r_{n_{min}}(\tau)} = \frac{S}{\sqrt{n_{max} - n_{min} + 1}} t_{1-\alpha/2, n_{max}-n_{min}} \tag{11b}$$

with significance level $\alpha = 0.05$ and $n_{max} - n_{min}$ degrees of freedom, Fig. 2c. From here the accuracy of the n_{min} independent average cluster radius, $\overline{R(\tau)}$, can be estimated using the corresponding $r_{n_{min}}$ (down-triangles and horizontal lines in Fig. 2c-b, respectively).

The shape of PDF function changes qualitatively for a medium, $\epsilon = -2.54$, and strong, $\epsilon = -4.23$, interactions, Fig. 3, comparing to the weak one. Namely, with an increase of time, the number of small clusters decreases in PDF, indicating that defects for the medium and strong interactions tend to be bound to clusters rather than remain as monomers. The peculiar PDF behavior is observed in the limit of a strong attraction and times larger than $\tau = 1.6{\times}10^5$. Despite the repeating calculations, ten times with the following averaging, the PDF function contains several long-living maxima for certain r values, e.g., $r_{15} = 0.35$ and $r_{22} = 0.39$ nm, Fig. 3b. These radii correspond to the stable clusters formed by magic defect cluster numbers $n = 15$ and $n = 22$, respectively. These

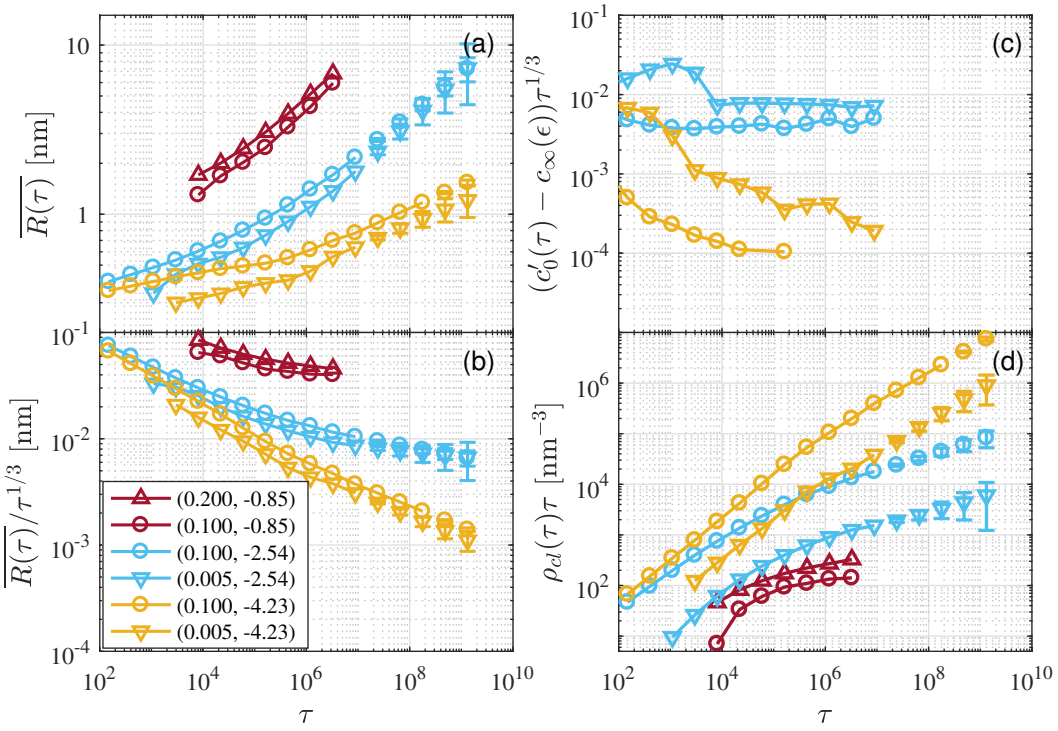

Figure 4: Average cluster radius (a) and LSW power law (b-d) asymptotic behavior. KMC simulations and the corresponding ARIMA(0,2,0) model forecasts are given with and without the solid lines, respectively. Defect concentration and dimensionless interactions are given as pairs (c_A, $\epsilon = \varepsilon/(k_BT)$). All data are obtained as average over 10 independent KMC simulations except (0.1,-0.85) case where a single calculation is performed. We use $L = 80a_0$ for (0.1,-4.23) and (0.1,-2.54); $L = 140a_0$ for (0.005,-4.23) and (0.005,-2.54); $L = 180a_0$ for (0.2,-0.85) and $L = 240a_0$ for (0.1,-0.85).

clusters are formed by the {110}–facets where each surface defect has six NN (and four NN at edges), that require more time to be disassembled, see insets in Fig. 3b.

4.3. Power laws

Let us now analyse quantitatively the cluster growth kinetic. Earlier different kinetic laws, $\overline{R(\tau)} \sim t^{1/p}$, have been proposed for different limiting cases: viscous flow ($p = 1$), interfacial control ($p = 2$), volume diffusion ($p = 3$), interfacial diffusion ($p = 4$), and pipe diffusion ($p = 5$) [44], respectively. Our KMC simulations correspond to the volume (3D, $p = 3$) diffusion case and thus the long-time behavior of the Ostwald ripening process is predicted by three power laws of the LSW theory

$$\overline{R(\tau)} \propto k_1\tau^{1/3} = k_1' t^{1/3}\,, \tag{12a}$$

$$c_0'(\tau) - c_\infty(\epsilon) \propto k_2\tau^{-1/3} = k_2' t^{-1/3}\,, \tag{12b}$$

$$\rho_{cl}(\tau) \propto k_3\tau^{-1} = k_3' t^{-1}\,, \tag{12c}$$

for average cluster radius, degree of supersaturation and cluster density [23, 39, 42], respectively. Equations (12) are valid for $\overline{R(\tau)} \gg R_{c0}$, where the initial critical radius for coalescence corresponding to the starting supersaturation is $R_{c0} = l_c c_\infty(\epsilon)/(c_0'(0) - c_\infty(\epsilon))$ [23]. This condition is fulfiled in our simulations and we neglect the R_{c0} contribution in Eq. (12).

The increase of average cluster radius, $\overline{R(\tau)}$, with time in KMC simulations demonstrates strong dependence on defect interaction energy, ϵ, Fig. 4a. The errors of the

KMC estimates are of the order of figure symbols and therefore not shown on the plot. A weak attraction leads to a faster growth of clusters than a strong one, due to shorter time needed for defects to detach from existing clusters, leading to a faster disappearance of small clusters and growth of the large ones. Contrary, a strong attraction increases time needed for defect detachment and thus slows down the large cluster growth at the expense of the small ones.

The KMC simulations show that cluster growth kinetics approaches the LSW long-time limit faster ($\tau > 10^6$) for weak interaction while for medium and strong interactions the long-time limit lies beyond our simulation times and could be estimated only from below using forecasting results $\tau > 10^8$ and $> 10^{10}$, respectively, Fig. 4b–d. By comparing the average cluster radius, rate of cluster growth and cluster concentration, Fig. 4a,b,d, one can conclude that the weak interaction leads to a small number of fast growing large clusters (Fig. 1b), while medium and strong interactions produce larger number of slower growing smaller clusters (Fig. 1c,d).

Defect concentration, c_A, plays a principal role in kinetics along with dimensionless interaction, ϵ, that determines the conditions for a cluster formation, Fig. 1. Thus, for a weak attraction and small concentration, $c_A = 0.005$, the cluster formation is absent. When cluster formation is possible, the defect concentration most strongly affects the cluster density in simulations, $c_A \propto \rho_{cl}$, Fig. 4d, while the average cluster radius and the radius growth rate are only slightly affected, Fig. 4a,b. The degree of supersaturation, Fig. 4c, for medium and strong interactions demonstrate the tendency towards saturation. It also implies that in the long-time limit the disparities arising for different concentrations disappear and monomer concentration (taking into account the cluster excluded volume), c_0', tends to the solubility concentration, $c_\infty(\epsilon)$, according to the LSW theory predictions. Unfortunately, the degree of supersaturation for a weak attraction remains undetermined (leading to unphysical result $c_0' < c_\infty(\epsilon)$) due to simplified bond counting model used in the interfacial energy, γ, estimate Eq. (5c), that is not applicable for loose clusters, Fig 1b.

Since the KMC simulations are limited by our computing capabilities, we performed the power law forecasting untill times $\tau = 10^9$, see symbols without line in Fig. 4a,b,d. The autoregressive moving average model has been applied earlier for analysis and simulation of time series containing noise, that arise, e.g., in tokamak experiments [45, 46]. In this paper, we use autoregressive integrated moving average ARIMA(p,d,q) model [22] that is well suited for nonstationary series. We found that the ARIMA(0,2,0) is the simplest parameter-free model that describe the KMC data,

$$y_\theta = 2y_{\theta-1} - y_{\theta-2} + \zeta_\theta, \tag{13}$$

where y and θ are the corresponding KMC simulation data in the logarithmic form and logarithmic time step index, respectively, and ζ_θ is the noise term at step θ. The forecasting, $\hat{y}_{\theta+h}$, for h steps ahead can be done using Eq. (13), see Fig. 4, with the following accuracy estimate [22]

$$\Delta\hat{y}_{\theta+h} = u_{\alpha/2}\left(1 + \sum_{k=1}^{h-1} k^2\right)^{1/2} s_\zeta, \tag{14}$$

where s_ζ is the standard deviation of the white noise process ζ_θ and $u_{\alpha/2}$ is the deviate exceeded by a proportion $\alpha/2$ of the unit normal distribution.

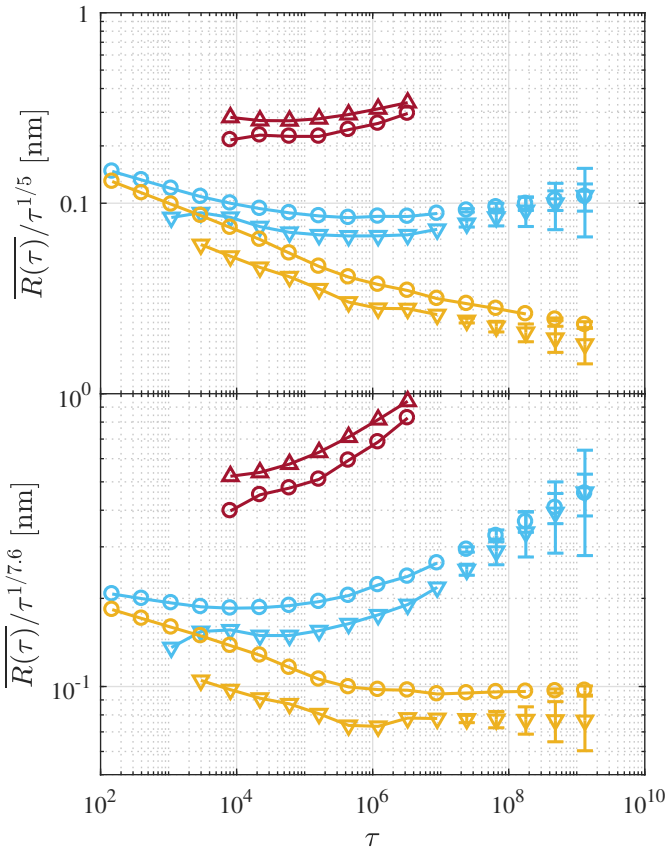

Figure 5: Average cluster radius scaling with different dimensionless time powers: (a) $p = 5$ (pipe diffusion) and (b) $p = 7.6$ (obtained from KMC results as an intermediate kinetics exponent for a strong interaction). The symbols in curves are the same as in Fig. 4.

Finally, we note that determination of the kinetics order p from the experimental data may be hindered by the transition (intermediate) type kinetics to the long-time limit. This is especially crucial in the limit of medium and strong interactions, when the intermediate kinetics may be observed at least untill times $\tau = 10^8$ and $\tau = 10^{10}$, respectively. When such data are scaled to the pipe diffusion order $p = 5$, they could demonstrate plateau-like behavior, Fig. 5a. Similarly to Eq. (12a), we can define

$$\overline{R(\tau)} \propto k_1'' t^{1/5}\,, \tag{15}$$

and estimate the corresponding cluster growth rate, k_1'', that are given below in Table 2.

For a strong interaction, we estimate the intermediate kinetics order $p = 7.6$ from KMC data and rescale the data in Fig. 5b to obtain the horizontal plateau for a strong interaction as expected. When comparing the intermediate kinetics regime (before reaching the LSW long-time limit with $p = 3$) for medium ($p = 5$ and $\tau \sim 10^6$) and strong ($p = 7.6$ and $\tau \sim 10^8$) interactions the ratio

$$\frac{\overline{R(\tau)}}{\tau^{1/p}} \approx 0.1[nm]\,, \tag{16}$$

is approximately constant and independent on the order p, defect interaction or concentration. Thus, the $\overline{R(\tau)}$ growth kinetics (order p) during the intermediate stage depends on the defect interaction – a stronger interaction leads to both larger exponent p and longer intermediate stage region.

5. A comparison of computer simulation results with LSW theory and experiments

Let us relate the dimensionless time τ to the typical physical (real) time of ODS steel processing, ranging from a few till several hundred of hours, Table 2. We find that $\tau = 10^7$ and $\tau = 1.3{\times}10^9$ (where for conversion we have used Y defect jump rate $\nu = 4{\times}10^3$ s^{-1} at temperature 1100 °C, see Table 1), lead to the estimates of 40 min and 90 h, respectively. The time of the order of 40 min is reached in KMC simulations, while 90 h limit is forecasted using ARIMA.

ARIMA forecasting allows us to estimate the system parameters on the order of several hundred hours, however the accuracy of the estimates are quickly reducing, Eq. (14). We can still observe that the medium attraction ($\epsilon = -2.54$) leads to the saturation behavior (long-time limit) for $\tau > 10^8$, whereas the strong interaction ($\epsilon = -4.23$) is unsaturated until $\tau < 10^9$.

The ARIMA forecast demonstrates that in the long-time limit the reaction rate, k_1' approaches the LSW theory for medium and strong interactions, Table 2.

The characteristic data of a cluster formation and growth (average cluster radius, cluster density and cluster growth rate) from the KMC simulation at experimentally relevant time and temperature limits from Fig. 4 are collected in Table 2. These characteristics can also be estimated from Eq. (12) in a long-time limit using coefficients predicted by the LSW theory [23]

$$\left(k_1'\right)^3 = k_1^3\nu = \frac{4}{9} D l_c c_\infty(\epsilon)\,, \tag{17a}$$

$$\left(k_2'\right)^{3/2} = k_2^{3/2}\nu^{-1/2} = \frac{3 l_c c_\infty(\epsilon)}{2\sqrt{D}}\,, \tag{17b}$$

$$k_3' = k_3\nu^{-1} = \left(2 D l_c c_\infty(\epsilon)\right)^{-1}\,. \tag{17c}$$

The average radius, $\overline{R(\tau)}$, and growth rate, k_1', predicted by the LSW theory agree well with the KMC data for a weak attraction ($\epsilon = -0.85$) (except the cluster density that is overestimated by two orders of magnitude), since simulations at times $\tau = 10^6$ have reached a long-time limit, Table 2. For medium and strong interactions the long-time limit is still unreached at $\tau = 10^7$, see Fig. 4a,b,d, that leads to an increasing disagreement between KMC simulation and predictions of the LSW theory, respectively. At the same time, the LSW theory supersaturation estimates, $k_2 = 7.4{\times}10^{-3}$ and $1.2{\times}10^{-4}$, agree well with the simulation data for medium and strong attractions, respectively, Fig. 4c.

The typical Y–O nano-clusters observed experimentally in ODS alloys have radii are a few nm and density of clusters around $10^{21} - 10^{23}$ m^{-3}, see Table 2. The recipes of sample preparations vary greatly. Alloys are obtained during a few hour processing, when the highest temperature achieved in the preparation stage is 1150 °C or 1050 °C, depending on the system, [5, 7]. The duration of HIPing stage is 4h [7]. Therefore, for a comparison with experimental values we scaled our KMC simulation results for temperature 1100 °C. Then, we can relate the dimensionless simulation time $\tau = 3{\times}10^6 - 10^7$ to the experimentally relevant time interval, of an order of an hour ($t = 13 - 40$ min).

There were also dedicated experiments [7, 9, 11, 12, 36] exceeding by several orders the typical annealing times of ≈ 2 h, performed at different temperatures, see Table 2. They were aimed at a study of cluster growth kinetics. It was shown that higher temperatures lead to larger clusters with smaller cluster density at increasing reaction rates.

Our KMC simulation results (radius 1.5 nm, density $7{\times}10^{23}$ m^{-3}, rate 0.25 nm/h$^{1/3}$) at strong interaction (-4.23) and small defect concentration (0.005) with ARIMA forecasting to 90 h at $T = 1100$ C agree quantitatively well with experimental values (radius 2.8 nm, density $5.8{\times}10^{22}$ m^{-3}, rate 0.53 nm/h$^{1/3}$) at $T = 1150$ C. One should note here that experimental temperature is by 50 C higher and annealing time is five times longer, 480 h that correspondingly increase the average cluster radius and decrease cluster density of the KMC simulations.

We have simulated concentration range in the KMC simulations from $c_A = 0.005$ up to 0.2, with maximum vs minimum ratio 40. Such system characteristics as cluster radius and growth rate are independent on concentration, Table 2. We observe that only the cluster density is highly sensitive to concentration, and then the KMC concentration $c_A = 0.005$, see Chapter 3, can be used for a comparison of results with experiments.

There is a general trend in experimental results that with a decrease of cluster average radii the cluster density increases, see Table 2 and earlier KMC simulations [13]. In our simulations decrease of cluster radius and increase of cluster density corresponds to an increase of attraction energies (or decrease of temperature). Alternatively, change of alloy composition by defects (e.g. Ti, Cr, and W) correspondingly affect the average interaction energy and thus corresponds to different KMC simulations with different average interactions.

In order to estimate the cluster growth rate in the Fe–14Cr–2W–0.1Ti–0.5%Fe_2Y and Fe–14Cr–2W–0.3Ti–0.3Y_2O_3 alloys annealing were performed up to 100 h at 1200 °C [7], see Table 2. It is found that the both growth rates are time independent ($k_1' = 0.22$ and 0.19 nm/h$^{1/3}$, respectively) and higher Ti concentration leads to smaller aggregate radius and larger density. Our interpretation, that the average defect interaction is increased with the higher Ti concentration (e.g., by comparing ARIMA forecasts for average ($\epsilon = -2.54$) and strong (-4.23) interactions in Table 2), allows to understand qualitatively these results.

The KMC simulations indicate that the cluster growth rate approaches the experimental value with an increase of attraction energy, ϵ, see Table 2: Stronger attraction decreases the cluster radius and increase the cluster density. The more so, the KMC results imply that for strong interactions the long-time limit is unreached and the system demonstrates the intermediate-kinetics with the specific power order $p = 7.6$ for a strong interaction ($\epsilon = -4.23$), Fig. 5.

6. Conclusions

We performed the KMC simulations, to model the yttrium oxide nano-cluster formation and growth in ODS steels. We have reduced the detailed microscopic oxide formation model to a single defect representing 3 types of defects: yttrium, oxygen atoms, Fe vacancies, that experience an attractive pairwise interaction. At the beginning of simulations defects are distributed homogeneously over the whole volume and are allowed to move with the jump rate of yttrium defects, known to be the slowest rate determining step.

Within this model, we have established the solubility–supersolubility phase diagram that (in the defect concentration and attraction energy (temperature) space) separates the unstable zone of a cluster formation from a stable region, where cluster formation is suppressed. Three prototypical defect attraction energies – weak, medium and strong – lead to formation of loose or compact {110}–faceted shape nano-clusters depending on interaction strength.

The methodology is developed for a defect distribution function analysis, that allows to separate the clusters with the Ostwald ripening from contribution of small unstable clusters. It is of a particular importance for weak attraction (high temperature) case: this allows us to follow quantitatively the nano-cluster formation process relevant for ODS steel production. In particular, cluster growth characteristics (cluster radius, growth rate, degree of solubility and density) obtained from KMC well agree with the Lifshitz-Slyozov-Wagner (LSW) theory predictions. The results for the weak attraction reach the LSW predicted long-time behavior during the typical for ODS steel production time of the order of an hour. However, such a weak interaction results differ strongly from the experiments suggesting that the average interaction between defects in real materials exceeds 0.1 eV.

Our KMC simulation model based on homogeneous nucleation is the simplest assumption that mimics nano-cluster formation in ODS steels. Despite its simplicity, it could provide quantitative estimates and experiment interpretation. KMC simulations demonstrate that for both medium and strong attractions the long-time limit is still unreached in a few hours (a typical ODS steel processing time). Instead, the system demonstrates new intermediate kinetics that is characterized by different orders p depending on interaction energy, for $\overline{R} \sim t^{1/p}$. Thus, for a strong attraction (0.5 eV) that quantitatively resemble the experimental results, we find that $p = 7.6$. The present simple model could be useful for a wide class of systems regarded as many-particle ensembles ranging from numerous physical applications to biological systems [47].

Acknowledgements

This work has been carried out within the framework of the EUROfusion Consortium and has received funding from the Euratom research and training programme 2014-2018 under grant agreement No 633053. The views and opinions expressed herein do not necessarily reflect those of the European Commission.

References

[1] G. Odette, M. Alinger, B. Wirth, Recent developments in irradiation-resistant steels, Annu. Rev. Mater. Res. 38 (2008) 471–503. doi:10.1146/annurev.matsci.38.060407.130315.

[2] G. R. Odette, Recent progress in developing and qualifying nanostructured ferritic alloys for advanced fission and fusion applications, JOM 66 (12) (2014) 2427–2441. doi:10.1007/s11837-014-1207-5.

[3] L. Dai, Y. Liu, Z. Dong, Size and structure evolution of yttria in ODS ferritic alloy powder during mechanical milling and subsequent annealing, Powder Technol. 217 (2012) 281–287. doi:10.1016/j.powtec.2011.10.039.

[4] M. Brocq, B. Radiguet, S. Poissonnet, F. Cuvilly, P. Pareige, F. Legendre, Nanoscale characterization and formation mechanism of nanoclusters in an ODS steel elaborated by reactive-inspired ball-milling and annealing, J. Nucl. Mater. 409 (2) (2011) 80–85. doi:10.1016/j.jnucmat.2010.09.011.

[5] A. London, S. Santra, S. Amirthapandian, B. Panigrahi, R. Sarguna, S. Balaji, R. Vijay, C. Sundar, S. Lozano-Perez, C. Grovenor, Effect of Ti and Cr on dispersion,

structure and composition of oxide nano-particles in model ODS alloys, Acta Mater. 97 (2015) 223–233. doi:10.1016/j.actamat.2015.06.032.

[6] S. V. Rogozhkin, N. N. Orlov, A. A. Nikitin, A. A. Aleev, A. G. Zaluzhnyi, M. A. Kozodaev, R. Lindau, A. Möslang, P. Vladimirov, Nanoscale characterization of 13.5% Cr oxide dispersion strengthened steels with various titanium concentrations, Inorg. Mater. Appl. Res. 6 (2) (2015) 151–155. doi:10.1134/S2075113315020136.

[7] C. A. Williams, G. D. Smith, E. A. Marquis, The effect of Ti on the coarsening behavior of oxygen-rich nanoparticles in oxide-dispersion-strengthened steels after annealing at 1200 °C, Scr. Mater. 67 (1) (2012) 108–111. doi:10.1016/j.scriptamat.2012.03.035.

[8] C. A. Williams, P. Unifantowicz, N. Baluc, G. D. Smith, E. A. Marquis, The formation and evolution of oxide particles in oxide-dispersion-strengthened ferritic steels during processing, Acta Mater. 61 (6) (2013) 2219–2235. doi:10.1016/j.actamat.2012.12.042.

[9] J. Shen, H. Yang, Y. Li, S. Kano, Y. Matsukawa, Y. Satoh, H. Abe, Microstructural stability of an as-fabricated 12Cr-ODS steel under elevated-temperature annealing, J. Alloy. Compd. 695 (2017) 1946–1955. doi:10.1016/j.jallcom.2016.11.029.

[10] M. Dadé, J. Malaplate, J. Garnier, F. D. Geuser, N. Lochet, A. Deschamps, Influence of consolidation methods on the recrystallization kinetics of a Fe14Cr based ODS steel, J. Nucl. Mater. 472 (2016) 143–152. doi:10.1016/j.jnucmat.2016.01.019.

[11] N. Cunningham, M. Alinger, D. Klingensmith, Y. Wu, G. Odette, On nano-oxide coarsening kinetics in the nanostructured ferritic alloy MA957: A mechanism based predictive model, Mater. Sci. Eng. A 655 (2016) 355–362. doi:10.1016/j.msea.2015.12.074.

[12] N. Cunningham, Y. Wu, D. Klingensmith, G. Odette, On the remarkable thermal stability of nanostructured ferritic alloys, Mater. Sci. Eng. A 613 (2014) 296–305. doi:10.1016/j.msea.2014.06.097.

[13] C. Hin, B. D. Wirth, J. B. Neaton, Formation of Y_2O_3 nanoclusters in nanostructured ferritic alloys during isothermal and anisothermal heat treatment: A kinetic Monte Carlo study, Phys. Rev. B 80 (2009) 134118. doi:10.1103/PhysRevB.80.134118.

[14] D. Murali, B. Panigrahi, M. Valsakumar, C. Sundar, Diffusion of Y and Ti/Zr in bcc iron: A first principles study, J. Nucl. Mater. 419 (1-3) (2011) 208–212. doi:10.1016/j.jnucmat.2011.05.018.

[15] L. Barnard, N. Cunningham, G. Odette, I. Szlufarska, D. Morgan, Thermodynamic and kinetic modeling of oxide precipitation in nanostructured ferritic alloys, Acta Mater. 91 (2015) 340–354. doi:10.1016/j.actamat.2015.03.014.

[16] X. Boulnat, M. Perez, D. Fabrgue, S. Cazottes, Y. de Carlan, Characterization and modeling of oxides precipitation in ferritic steels during fast non-isothermal consolidation, Acta Mater. 107 (2016) 390–403. doi:10.1016/j.actamat.2016.01.034.

[17] G. Zvejnieks, V. N. Kuzovkov, Monte Carlo simulations for a Lotka-type model with reactant surface diffusion and interactions, Phys. Rev. E 63 (2001) 051104. doi:10.1103/PhysRevE.63.051104.

[18] E. Tornau, V. Petrauskas, G. Zvejnieks, Surface phase transitions at O and CO catalytic reaction on Pd(1 1 1), Catal. Today 116 (1) (2006) 62–68. doi:10.1016/j.cattod.2006.02.081.

[19] G. Zvejnieks, V. Kuzovkov, V. Petrauskas, E. Tornau, Modelling of phase transitions and reaction at CO adsorption on oxygen precovered Pd(1 1 1), Appl. Surf. Sci. 252 (15) (2006) 5395–5398. doi:10.1016/j.apsusc.2005.12.048.

[20] G. Zvejnieks, A. Ibenskas, E. Tornau, Effects of pressure, temperature and atomic exchanges on phase separation dynamics in Au/Ni(111) surface alloy: Kinetic Monte Carlo study, J. Alloy. Compd. 649 (2015) 313–319. doi:10.1016/j.jallcom.2015.07.132.

[21] G. Zvejnieks, P. Merzlyakov, V. Kuzovkov, E. Kotomin, Void lattice formation in electron irradiated CaF_2: Statistical analysis of experimental data and cellular automata simulations, Nucl. Instr. Meth. B 368 (2016) 138–143. doi:10.1016/j.nimb.2015.11.037.

[22] G. E. P. Box, G. M. Jenkins, G. C. Reinsel, G. M. Ljung, Time Series Analysis: Forecasting and Control (Fifth Edition), John Wiley and Sons Inc., Hoboken, New Jersey, 2015.

[23] I. Lifshitz, V. Slyozov, The kinetics of precipitation from supersaturated solid solutions, J. Phys. Chem. Solids 19 (1–2) (1961) 35–50. doi:10.1016/0022-3697(61)90054-3.

[24] C. Wagner, Theorie der Alterung von Niederschlägen durch Umlösen (Ostwald-Reifung), Z. Elektrochem. 65 (7-8) (1961) 581–591.
URL http://onlinelibrary.wiley.com/doi/10.1002/bbpc.19610650704/full

[25] J. Schmelzer, D. P. Landau, Monte Carlo simulation of nucleation and growth in the 3D nearest-neighbor Ising model, Int. J. Mod. Phys. C 12 (03) (2001) 345–359. doi:10.1142/S012918310100178X.

[26] G. Barenblatt, Scaling, Self-similarity, and Intermediate Asymptotics: Dimensional Analysis and Intermediate Asymptotics, Cambridge Texts in Applied Mathematics, Cambridge University Press, 1996.

[27] Y. B. Zel'dovich, D. D. Sokolov, Fractals, similarity, intermediate asymptotics, Soviet Physics Uspekhi 28 (7) (1985) 608–616. doi:10.1070/PU1985v028n07ABEH003873.

[28] S. Piskunov, G. Zvejnieks, Y. F. Zhukovskii, S. Bellucci, Atomic and electronic structure of both perfect and nanostructured Ni(111) surfaces: First-principles calculations, Thin Solid Films 519 (11) (2011) 3745–3751. doi:10.1016/j.tsf.2011.01.357.

[29] G. Zvejnieks, A. Ibenskas, E. Tornau, Kinetic Monte Carlo modeling of reaction-induced phase separation in Au/Ni(111) surface alloy, Surf. Coat. Tech. 255 (2014) 15–21. doi:10.1016/j.surfcoat.2013.11.002.

[30] M. Alinger, B. Wirth, H.-J. Lee, G. Odette, Lattice Monte Carlo simulations of nanocluster formation in nanostructured ferritic alloys, J. Nucl. Mater. 367370, Part A (2007) 153–159. doi:10.1016/j.jnucmat.2007.03.010.

[31] C. Hin, B. Wirth, Formation of oxide nanoclusters in nanostructured ferritic alloys during anisothermal heat treatment: A kinetic Monte Carlo study, Mater. Sci. Eng. A 528 (45) (2011) 2056–2061. doi:10.1016/j.msea.2010.11.017.

[32] P. Jegadeesan, D. Murali, B. K. Panigrahi, M. C. Valsakumar, C. S. Sundar, Lattice kinetic Monte Carlo simulation of Y-Ti-O nanocluster formation in bcc Fe, Int. J. Nanosci. 10 (04n05) (2011) 973–977. doi:10.1142/S0219581X11008691.

[33] F. Hanic, M. Hartmanová, G. G. Knab, A. A. Urusovskaya, K. S. Bagdasarov, Real structure of undoped Y_2O_3 single crystals, Acta Cryst. 40 (2) (1984) 76–82. doi:10.1107/S0108768184001774.

[34] W. P. Davey, Precision measurements of the lattice constants of twelve common metals, Phys. Rev. 25 (1925) 753–761. doi:10.1103/PhysRev.25.753.

[35] L. Kittiratanawasin, R. Smith, B. P. Uberuaga, K. E. Sickafus, Radiation damage and evolution of radiation-induced defects in Er_2O_3 bixbyite, J. Phys.: Condens. Matter 21 (11) (2009) 115403. doi:10.1088/0953-8984/21/11/115403.

[36] M. Alinger, On the formation and stability of nanometer scale precipitates in ferritic alloys during processing and high temperature service, Ph.D. thesis, University of California, Santa Barbara (September 2004).

[37] V. Kuzovkov, G. Zvejnieks, Reply to "Comment on 'Monte Carlo simulations for a Lotka-type model with reactant surface diffusion and interactions' ", Phys. Rev. E 65 (2002) 033102. doi:10.1103/PhysRevE.65.033102.

[38] J. Mullin, Solutions and solubility, in: J. Mullin (Ed.), Crystallization (Fourth Edition), Butterworth-Heinemann, Oxford, 2001, pp. 86–134. doi:10.1016/B978-075064833-2/50005-X.

[39] A. Baldan, Review Progress in Ostwald ripening theories and their applications to nickel-base superalloys Part I: Ostwald ripening theories, J. Mater. Sci. 37 (11) (2002) 2171–2202. doi:10.1023/A:1015388912729.

[40] M. Strobel, K.-H. Heinig, W. Möller, Three-dimensional domain growth on the size scale of the capillary length: Effective growth exponent and comparative atomistic and mean-field simulations, Phys. Rev. B 64 (2001) 245422. doi:10.1103/PhysRevB.64.245422.

[41] C. D. Lorenz, R. M. Ziff, Precise determination of the bond percolation thresholds and finite-size scaling corrections for the sc, fcc, and bcc lattices, Phys. Rev. E 57 (1998) 230–236. doi:10.1103/PhysRevE.57.230.

[42] P. W. Voorhees, The theory of Ostwald ripening, J. Stat. Phys. 38 (1) (1985) 231–252. doi:10.1007/BF01017860.

[43] G. A. Korn, T. M. Korn, Mathematical Handbook for Scientists and Engineers: Definitions, Theorems, and Formulas for Reference and Review, Dover Publications, Inc., Mineola, New York, 2000.

[44] H. Gleiter, Microstructure, in: R. W. Cahn, P. Haasen (Eds.), Physical Metallurgy (Fourth Edition), North-Holland, Oxford, 1996, pp. 843–942. doi:10.1016/B978-044489875-3/50014-4.

[45] G. Zvejnieks, V. N. Kuzovkov, O. Dumbrajs, A. W. Degeling, W. Suttrop, H. Urano, H. Zohm, Autoregressive moving average model for analyzing edge localized mode time series on Axially Symmetric Divertor Experiment (ASDEX) Upgrade tokamak, Phys. Plasmas 11 (12) (2004) 5658–5667. doi:10.1063/1.1814368.

[46] A. W. Degeling, J. B. Lister, Y. R. Martin, G. Zvejnieks, Were the chaotic ELMs in TCV the result of an ARMA process?, Plasma Phys. Contr. F. 46 (10) (2004) L15–L21. doi:10.1088/0741-3335/46/10/L01.

[47] R. Mahnke, J. Kaupužs, I. Lubashevsky, Physics of Stochastic Processes: How Randomness Acts in Time, Wiley-VCH Verlag GmbH & Co. KGaA, Weinheim, 2009.

			$\overline{R(\tau)}$ [nm]	$\rho_{cl}(\tau)$ [m^{-3}]	k_1' [$nm/h^{1/3}$]	k_1'' [$nm/h^{1/5}$]	Annealing conditions
KMC simulation results:							
c_A	ϵ	τ					
0.100	−0.85	3×10^6	6	5×10^{22}	9.7	8.1	1100C, 13min
0.100 0.005	−2.54	10^7	2.0	2×10^{24} 2×10^{23}	2.4	2.2	1100C, 40min
0.100 0.005	−4.23	10^7	0.7	4×10^{25} 4×10^{24}	0.9	0.8	1100C, 40min
ARIMA(0,2,0) forecasts:							
0.100 0.005	−2.54	1.3×10^9	7.0	6×10^{22} 5×10^{21}	1.5	2.7	1100C, 90h
0.100 0.005	−4.23	1.3×10^9	1.5	5×10^{24} 7×10^{23}	0.25	0.54	1100C, 90h
LSW results:							
	ϵ	$z_s - z_b$					
	−0.85	−2	5	10^{24}	8		1100C, 13min
	−2.54	−2	1.1	10^{26}	1.2		1100C, 40min
	−4.23	−2	0.14	10^{29}	0.15		1100C, 40min
Experimental results:							
Fe–12Cr–2W–0.3Ti–0.25Y_2O_3 [a]			9.2	2×10^{21}	3.1		1400C, 24h
Fe–12Cr–2W–0.3Ti–0.25Y_2O_3 [a]			4.5	10^{22}	1.4		1300C, 24h
Fe–12Cr–2W–0.3Ti–0.25Y_2O_3 [a]			2.6	10^{23}	0.8		1200C, 24h
Fe–14Cr–0.3Mo–Ti–0.25Y_2O_3 [b]			6.5	5.2×10^{21}	3.4	4.4	1400C, 9h
Fe–14Cr–0.3Mo–Ti–0.25Y_2O_3 [b]			4.2	2.2×10^{22}	1.7	2.4	1300C, 27h
Fe–14Cr–0.3Mo–Ti–0.25Y_2O_3 [b]			3.7	1.8×10^{22}	0.53	1.11	1200C, 480h
Fe–14Cr–0.3Mo–Ti–0.25Y_2O_3 [b]			2.8	5.8×10^{22}	0.53	0.80	1150C, 480h
Fe–14Cr–0.3Mo–Ti–0.25Y_2O_3 [b]			1.5	4.7×10^{23}	0.052	0.22	1000C, 21.9kh
Fe–14Cr–2W–0.1Ti–0.5Fe_2Y [c]			3.8 *	4.3×10^{22} *	0.22		1200C, 100h
Fe–14Cr–2W–0.3Ti–0.3Y_2O_3 [c]			2.5 *	7.1×10^{23} *	0.19		1200C, 100h
Fe–0.3Y_2O_3 [d]			4.8	8×10^{21}			950C, 2h
Fe–0.2Ti–0.3Y_2O_3 [d]			3.9	1.1×10^{23}			950C, 2h
Fe–14Cr–0.2Ti–0.3Y_2O_3 [d]			1.9	2.6×10^{23}			750C, 2h

Table 2: KMC simulation result estimates from Fig. 4 at times $\tau = 3\times10^6$ (t = 13 min) and $\tau = 10^7$ (t = 40 min), respectively, where for conversion we have used Y defect jump rate $\nu = 4\times10^3$ s^{-1} at temperature 1100 °C, see Table 1. The LSW theory predictions are obtained from Eq. (17). [a]Data are taken from Ref. [9]. [b]Data for alloy MA957 are from Ref. [11, 12, 36]. Experimental estimates[c,d] are from Refs. [7] and [5], respectively. *Values are given for samples before the 100h annealing.